Magnetotransport properties of epitaxial films and Hall bar devices of the correlated layered ruthenate $Sr_3Ru_2O_7$

Prosper Ngabonziza [1,2,*] Anand Sharma [1] Anna Scheid [3] Sethulakshmi Sajeev,[1]
Peter A. van Aken [3] and Jochen Mannhart [3]

[1]*Department of Physics & Astronomy, Louisiana State University, Baton Rouge, Louisiana 70803, USA*
[2]*Department of Physics, University of Johannesburg, P.O. Box 524 Auckland Park 2006, Johannesburg, South Africa*
[3]*Max Planck Institute for Solid State Research, Heisenbergstr. 1, 70569 Stuttgart, Germany*

For epitaxial $Sr_3Ru_2O_7$ films grown by pulsed laser deposition, we report a combined structural and magneto-transport study of thin films and Hall bar devices patterned side-by-side on the same film. Structural properties of these films are investigated using x-ray diffraction and high-resolution transmission electron microscopy, and confirm that these films are epitaxially oriented and nearly phase pure. For magnetic fields applied along the c axis, a positive magnetoresistance of 10% is measured for unpatterned $Sr_3Ru_2O_7$ films, whereas for patterned Hall bar devices of channel widths of 10 and 5 µm, magnetoresistance values of 40% and 140% are found, respectively. These films show switching behaviors from positive to negative magnetoresistance that are controlled by the direction of the applied magnetic field. The present results provide a promising route for achieving stable epitaxial synthesis of intermediate members of correlated layered strontium ruthenates, and for the exploration of device physics in thin films of these compounds.

I. INTRODUCTION

Layered ruthenates are peculiar strongly correlated materials in which several comparable interactions compete to give rise to a variety of novel electronic and magnetic phenomena. Intricate phenomena observed in layered ruthenates range from superconductivity [1] to emergent ferromagnetism and insulator-metal transitions [2], to colossal and large magnetoresistance [3], and other electron- and spin-ordering states [4]. The layered strontium ruthenates of the Ruddlesden-Popper (R-P) phases, $Sr_{n+1}Ru_nO_{3n+1}$ ($n = 1, 2, 3, \infty$), play a pivotal role in the study of strongly correlated electron systems. Depending on the number n of the RuO_6 octahedra layers in the unit cell, the phenomena obtained in these systems include potentially unconventional superconductivity in Sr_2RuO_4 ($n = 1$) [1,5–7], metamagnetic quantum criticality and electron nematic fluid in $Sr_3Ru_2O_7$ ($n = 2$) [8–11], orbital-dependent double metamagnetic transition and characteristics of Hund's metal correlations in $Sr_4Ru_3O_{10}$ ($n = 3$) [12–15], and itinerant ferromagnetism coexisting with localized correlated behavior in $SrRuO_3$ ($n = \infty$) [16–19]. The rich array of distinct collective phenomena in these materials show that $Sr_{n+1}Ru_nO_{3n+1}$ are attractive for exploring the rich physics of strongly correlated layered materials.

Beyond fundamental interests, the potential of $Sr_{n+1}Ru_nO_{3n+1}$ for applied physics has driven interests in thin films, particularly in Sr_2RuO_4 ($n = 1$) films due to its unconventional superconductivity and Shubnikov-de Haas effect [20,21], and in $SrRuO_3$ ($n = \infty$) films as an excellent electrode material integrated in diverse oxide thin-film devices for a variety of oxide electronic and nanoionic applications [16,22], and also as a candidate Weyl semimetal magnetic material [23,24]. However, due to the complexity of synthesizing phase-pure epitaxial films of intermediate $Sr_{n+1}Ru_nO_{3n+1}$ members ($1 < n < \infty$), only a few papers reported attempts to epitaxially grow double- and triple-layered strontium ruthenate films, $Sr_3Ru_2O_7$ and $Sr_4Ru_3O_{10}$ [10,25]. Understanding the synthesis science of epitaxial films of these intermediate members provides a unique opportunity for further explorations of their correlated phases in thin films and devices. Also, the precise control of their functional interfaces at the atomic level will open new routes towards the realization of novel interface-induced functionalities in correlated layered ruthenates, which would otherwise not be accessible when using single crystals.

We focus on epitaxial films of the bilayer strontium ruthenate $Sr_3Ru_2O_7$. The material $Sr_3Ru_2O_7$ is an enhanced Pauli paramagnet in its ground state that undergoes an anisotropic metamagnetic transition (i.e., a sudden increase in the magnetization within a small change of applied magnetic field) [26,27]. Under magnetic field applied in the out-of-plane direction, $Sr_3Ru_2O_7$ displays unusual double metamagnetic transitions at critical magnetic fields of $\sim$8 T and 13.5 T [28]. However, for in-plane magnetic fields parallel to the ruthenium oxygen planes, metamagnetic behaviors shift to a lower critical field of $\sim$5.5 T [27]. In magnetotransport, a peak in the magnetoresistance (MR) has been observed around 5 T under in-plane applied magnetic fields, and it has been attributed to originate from in-plane metamagnetic behavior of $Sr_3Ru_2O_7$ [10,29,30]. Metamagnetic transitions in

*pngabonziza@lsu.edu

double- and triple-layered ruthenates have been proposed to arise from magnetic fluctuations due to the presence of flat bands near the Fermi level in the electronic band dispersions [15,31–35]. Also, electron nematic behaviors [36], ascribed to a spin-dependent symmetry-breaking Fermi surface distortion, have been observed both in single crystals and strained epitaxial films of $Sr_3Ru_2O_7$ [8,10,29].

Although magnetotransport properties of $Sr_3Ru_2O_7$ have been characterized both in bulk single crystals [37], single crystalline nanosheets [30], and in compressively strained epitaxial films [10], little is known about the MR characteristics of epitaxial $Sr_3Ru_2O_7$ films and thin-film devices patterned side-by-side on the same film. Such epitaxial films are ideal for the exploration of lateral dimensional confinement effects in epitaxial films for tuning their electronic ground states. Also, having various micro- and nanoscale devices fabricated side-by-side on the same film provides an advantage over single crystal-based devices, because it provides the opportunity to perform comparative study of magnetotransport properties from the same sample, measured in similar conditions.

In this paper, we report on the epitaxy of $Sr_3Ru_2O_7$ thin films, as well as on the magnetotransport trends of epitaxial films and Hall bar devices of $Sr_3Ru_2O_7$. The synthesis of near phase-pure $Sr_3Ru_2O_7$ films was previously reported, but only for epitaxial films grown by molecular beam epitaxy (MBE) [10,25]. Here, we use pulsed laser deposition (PLD) for the epitaxial growth of these thin films. First, we focus on optimizing the PLD growth conditions for achieving phase-pure epitaxial $Sr_3Ru_2O_7$ films. Subsequent structural analyses of these samples, using x-ray diffraction (XRD) and high-resolution scanning transmission electron microscopy (STEM), confirm that these films are epitaxially oriented and nearly phase pure. From magnetization characterization, the $Sr_3Ru_2O_7$ films show no ferromagnetic transition over the entire measured temperature range. Second, for epitaxial films prepared at optimal growth conditions, we fabricate side-by-side on the same $Sr_3Ru_2O_7$ sample several Hall bar devices of various channel widths, and then explore their electronic transport properties. We find that the sheet resistance of Hall bar devices increases as the active channel width of $Sr_3Ru_2O_7$ films decreases, while the sheet resistance of unpatterned films is higher than those of structured Hall bar devices. Lastly, we perform a comparative MR study of unpatterned epitaxial $Sr_3Ru_2O_7$ films and Hall bar devices. At low temperatures, for magnetic fields applied along the c axis ($B \parallel c$), with the excitation current perpendicular to the direction of applied field, MR values as high as 10% and up to 140% are achieved in unpatterned films and Hall bar devices, respectively. Furthermore, these films show switching behaviors from positive to negative MR that are controlled by the direction of the applied magnetic field.

II. THIN FILM EPITAXY

Figure 1(a) illustrates the epitaxy of $Sr_3Ru_2O_7$ films on a TiO_2-terminated $SrTiO_3$ substrate. All $Sr_3Ru_2O_7$ films were grown on (100)-oriented $SrTiO_3$ single crystalline substrates ($5 \times 5 \times 1$ mm^3) [Fig. 1(b)]. Prior to deposition, the $SrTiO_3$ substrates were terminated *in situ* using a CO_2 laser [38]. We deposited $Sr_3Ru_2O_7$ films using PLD by ablating a

stoichiometric $Sr_3Ru_2O_7$ target [39] with an excimer laser ($\lambda = 248$ nm) at 2 Hz up to a thickness of 25 nm at a deposition rate of ~ 15 Å min^{-1}. During growth, the molecular oxygen pressure in the chamber was kept at $P_{O_2} = 8.0 \times 10^{-2}$ mbar. Immediately after growth, under the same P_{O_2}, samples were cooled to room temperature at a cooling rate of 80 °C/min. To establish stable epitaxial growth conditions, we have prepared a series of $Sr_3Ru_2O_7$ films at various substrate temperatures (T_{sub}), from 680 to 800 °C in steps of 20 °C. The optimal substrate temperature for the epitaxial growth of $Sr_3Ru_2O_7$ films was found to be $T_{sub} = 720$ °C. At this temperature, we have also prepared a series of $Sr_3Ru_2O_7$ films varying the laser fluence from 1.5 to 3 J/cm^2 in steps of 0.5 J/cm^2, and better quality films were obtained at a laser fluence of 2.5 J/cm^2.

III. RESULTS AND DISCUSSION

The surface quality of epitaxial $Sr_3Ru_2O_7$ films was characterized by reflection high-energy electron diffraction (RHEED) and atomic force microscopy (AFM). The deposition of $Sr_3Ru_2O_7$ was in situ monitored by RHEED [Fig. 1(c)]. We observe that the intensity of time-dependent RHEED oscillations remains roughly the same throughout the deposition of the $Sr_3Ru_2O_7$ layers on $SrTiO_3$ substrates. The RHEED oscillations indicate that the $Sr_3Ru_2O_7$ films are grown in a layer-by-layer mode with a smooth surface as also demonstrated by sharp, diffracted, and specular RHEED patterns [inset in Fig. 1(c)]. After PLD growth, the surface morphology of the $Sr_3Ru_2O_7$ films was investigated using AFM. Figure 1(d) depicts a typical AFM image for a representative 25-nm-thick $Sr_3Ru_2O_7$ film. The surface of the resulting $Sr_3Ru_2O_7$ films at optimal substrate temperature is smooth and it exhibits well-pronounced terraces, demonstrating a high-quality surface morphology of these films. For a lateral scan size of $\sim 5 \times 5$ μm^2, the extracted surface roughness is $\leqslant 0.2$ nm for a 25-nm-thick $Sr_3Ru_2O_7$ film [bottom panel in Fig. 1(d)].

The crystalline quality and phase purity of $Sr_3Ru_2O_7$ films were characterized by XRD. Figure 2(a) shows representative θ–2θ scans for the $Sr_3Ru_2O_7$ films at various substrate temperatures and laser fluence. For the films grown at optimal growth conditions ($T_{sub} = 720$ °C and laser fluence $= 2.5$ J/cm^2), only the substrate peaks and phase-pure $00l$ family of the film diffraction peaks are resolved, which indicates a high crystallinity and verifies that the $Sr_3Ru_2O_7$ films were aligned along the c axis. The 002, 004, 008, 00$\underline{10}$, 00$\underline{12}$, 00$\underline{14}$, 00$\underline{20}$, and 00$\underline{22}$ Bragg diffraction peaks are well resolved, while the 006, 00$\underline{16}$, and 00$\underline{18}$ peaks are not present due to the small film thickness and the low structure factors of these peaks [10]. The extracted out-of-plane lattice parameter for epitaxial films grown at the optimal growth conditions is $c = 20.72$ Å. This value is consistent to the bulk c axis lattice constant of 20.7194 Å reported previously in single crystals of $Sr_3Ru_2O_7$ [30,40–42]. Extra phases, indicated by (#) in Fig. 2(a), were detected in $Sr_3Ru_2O_7$ films grown at high substrate temperatures, underlining the role of proper tuning of T_{sub} for achieving phase stability in these films. These extra phases are associated with the (00l) family of the diffraction
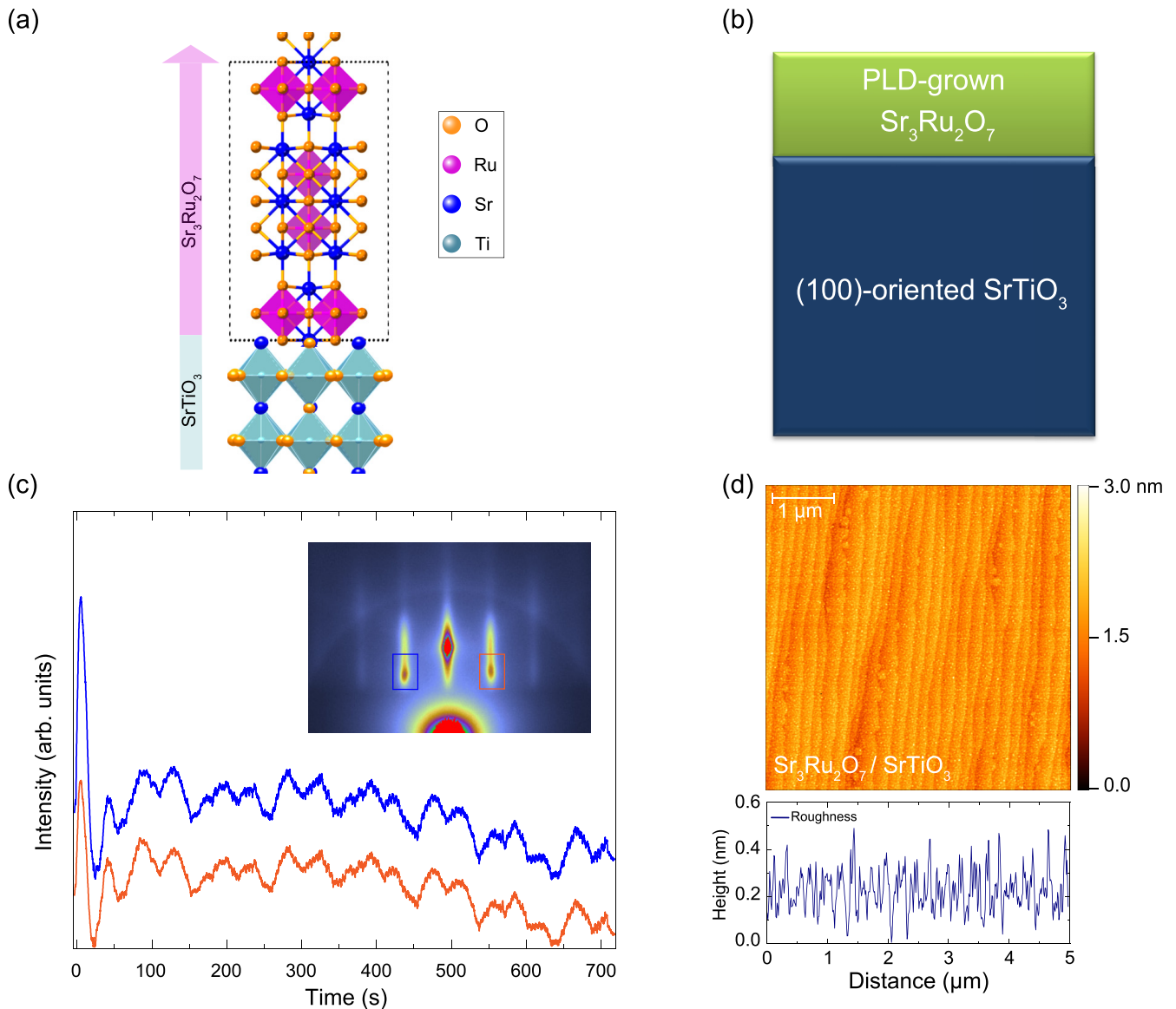
FIG. 1. Crystal structure and surface quality of epitaxial $Sr_3Ru_2O_7$ films. Schematic representation of (a) the crystal structure and (b) layout of the double-layered $Sr_3Ru_2O_7$ thin film grown by pulsed laser deposition on a (001)-oriented $SrTiO_3$ substrate. Dashed-line rectangle in (a) delineates the unit cell of $Sr_3Ru_2O_7$. (c) Time-dependent RHEED intensity oscillations recorded during the growth of 18-nm-thick $Sr_3Ru_2O_7$ film. The inset depicts RHEED patterns of a $Sr_3Ru_2O_7$ film, where the blue and orange rectangles mark the region from which the integrated intensity as a function of time was recorded during the deposition of $Sr_3Ru_2O_7$. (d) A representative AFM image displaying the surface morphology and (bottom panel) corresponding surface roughness profile of a typical $Sr_3Ru_2O_7$ film.

peaks (002, 008, and 00$\underline{14}$) of the $n = 1$ R-P phase [43,44], in agreement with STEM data (see Fig. S1 within the Supplemental Material, SM [45]).

Figure 2(b) shows a closeup view of the $\theta-2\theta$ scans around the 00$\underline{10}$ diffraction peak for the $Sr_3Ru_2O_7$ films grown at various T_{sub} and laser fluence. For the films grown at the optimal growth conditions, only the 00$\underline{10}$ peaks are resolved with noticeable thickness fringes, which highlight phase purity and smooth growth. However, we observed shifting of the 00$\underline{10}$ peaks to lower 2θ angles for films that were not grown at the optimal growth conditions. The shifting of the peak demonstrates that the c axis lattice constant expands, indicating intergrowth of other $Sr_{n+1}Ru_nO_{3n+1}$ phases and change of stability of the $Sr_3Ru_2O_7$ films. In particular, the $Sr_3Ru_2O_7$

films grown at $T_{sub} = 680°C$ exhibited a peak shoulder around the substrate peak, indicating an intergrowth of higher n R-P phases, with predominance of the $SrRuO_3$ phase [47]. These observations are consistent with the STEM data (see Fig. S1 within the SM [45]) in which considerable intergrowths of other n members of the $Sr_{n+1}Ru_nO_{3n+1}$ series were clearly detected for epitaxial $Sr_3Ru_2O_7$ films prepared outside the optimal growth conditions.

Figure 2(c) shows four reciprocal space maps (RSM) around the asymmetric pseudocubic $\bar{1}03_p$ reflection peak of the substrate for different ϕ angle orientations. From all four RSMs, it is evident that the $Sr_3Ru_2O_7$ film is fully epitaxially strained and single phase, as confirmed by extracted pseudocubic in-plane lattice constant of $a = 3.889$ Å. As the film
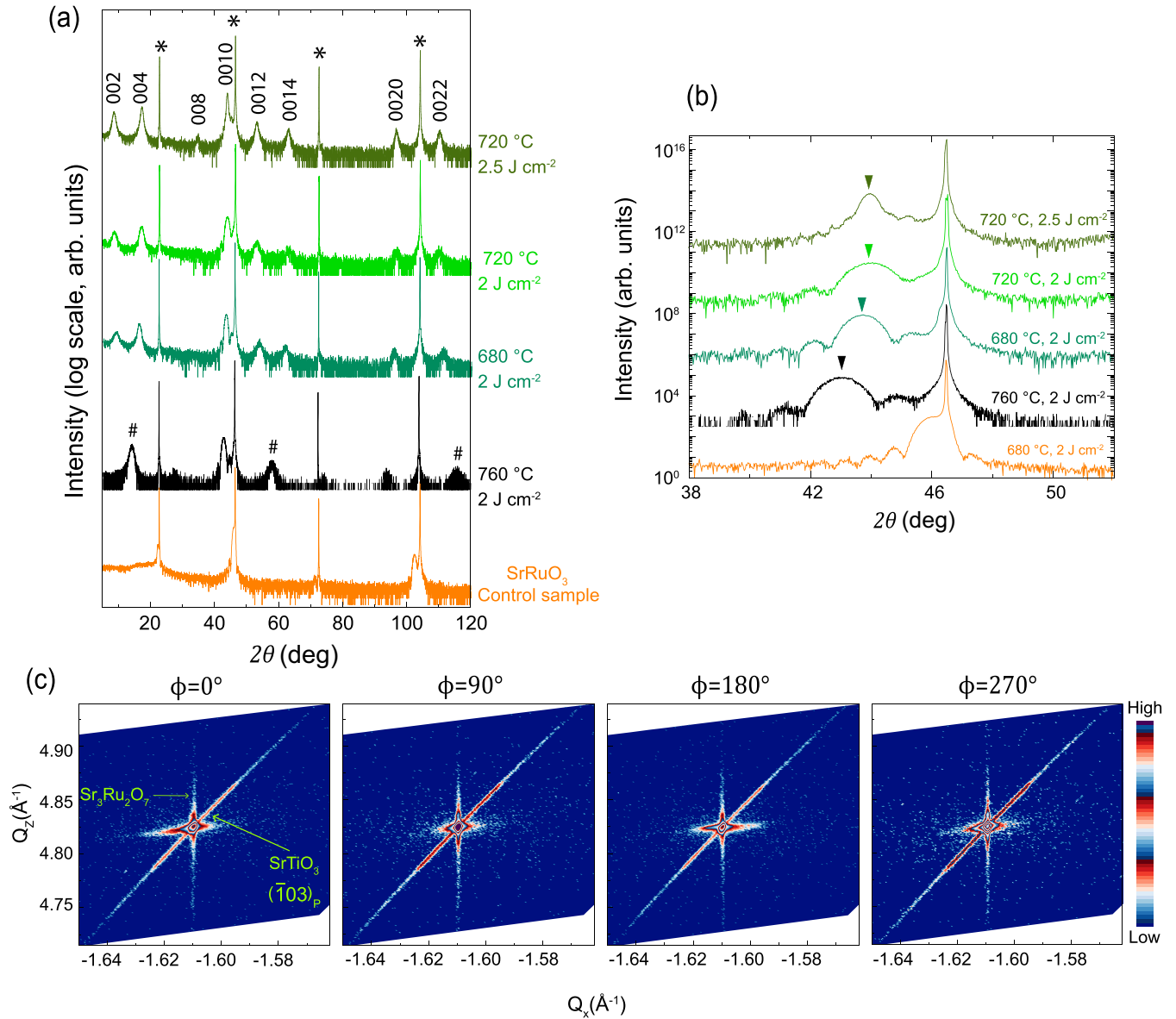
FIG. 2. Structural characterization of epitaxial $Sr_3Ru_2O_7$ films. (a) Representative XRD scans of 25-nm-thick $Sr_3Ru_2O_7$ films prepared at different growth temperatures and laser fluences together with a scan of a $SrRuO_3$ control film (orange curve). For films prepared at optimal substrate temperature (720 °C), only the $SrTiO_3$ Bragg's reflection peaks (*) and the 00*l* family of the $Sr_3Ru_2O_7$ films' diffraction peaks are resolved. Extra phases (#) in $Sr_3Ru_2O_7$ films are observed at high growth temperatures. (b) Closeup XRD patterns around the 00$\underline{10}$ peak of $Sr_3Ru_2O_7$. For growth temperatures higher or lower than 720 °C, the 00$\underline{10}$ peaks of $Sr_3Ru_2O_7$ shift to lower values. The Laue fringes in (b) indicate that there may be a thin layer of excess material, consistent with previous reports, which showed that excess material in the film of the order of a few angstroms will result in Laue fringes exhibiting clear differences [46]. (c) Reciprocal space maps for a $Sr_3Ru_2O_7$ film around the $\bar{1}03_p$ reflection of $SrTiO_3$ substrate, where *p* refers to pseudocubic indices, measured at four different ϕ angle orientations of the $SrTiO_3$ substrate.

peak is very close to the $\bar{1}03_p$ reflection of the substrate, potential overlap of the truncation rod from the substrate with the film peak could affect a precise extraction of in-plane lattice parameter. The extracted in-plane lattice parameter is close to reported lattice parameter (∼3.890 Å) of $Sr_3Ru_2O_7$ bulk single crystals [40,41]. Although the epitaxial films appear to be single phase from XRD characterization, it is also essential to use transmission electron microscopy (TEM) to check for intergrowths that are known to be difficult to discern in XRD patterns of layered R-P materials [25,48,49].

To provide a complementary real-space microstructural characterization of these films, cross-sectional TEM imaging was performed. With these studies, we investigated the defect populations of these films including possible intergrowths of $n \neq 2$ members of the $Sr_{n+1}Ru_nO_{3n+1}$ series. Figure 3(a) depicts a cross-sectional STEM image of the entire film thickness of a representative $Sr_3Ru_2O_7$ film prepared at the optimal growth conditions. For films prepared at the optimal substrate temperature, no surface steps at the substrate and defects throughout the entire film thickness were observed.
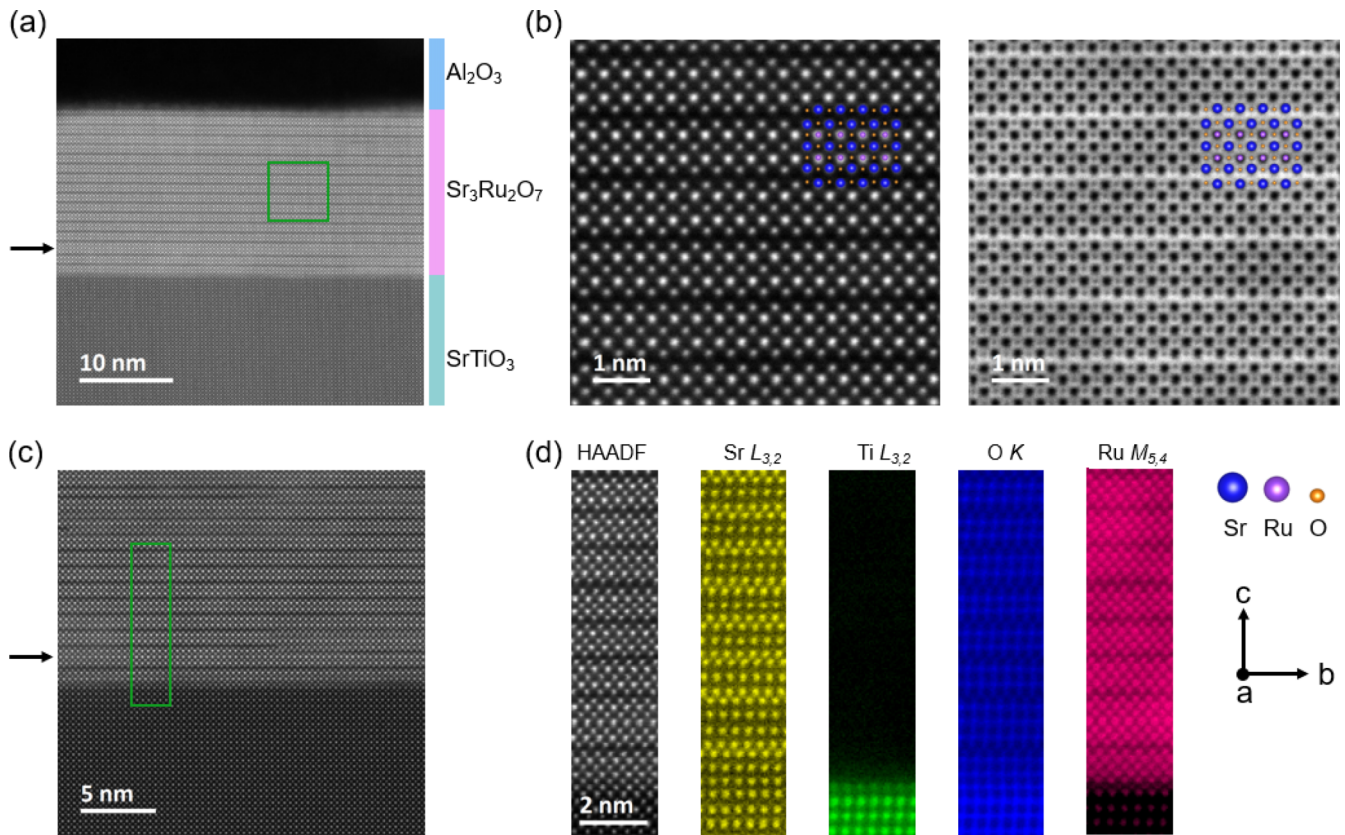
FIG. 3. Microstructural characterization of representative $Sr_3Ru_2O_7$ films prepared at optimal growth conditions. (a) Overview scanning transmission electron microscopy (STEM) image of $Sr_3Ru_2O_7$ in [100] zone axis orientation. (b) The magnified annular dark-field (center) and annular bright-field (right) images show the film with a good structural order. A schematic atomic structural model, displaying the sequence of Sr, Ru, and O atoms is shown, overlaying the resolved double-layered atomic structure. (c) High-resolution STEM image of a $Sr_3Ru_2O_7$ film in [100] orientation together with corresponding (d) electron energy-loss spectroscopy (EELS) elemental mapping of the $Sr_3Ru_2O_7/SrTiO_3$ interface showing the elemental distribution in the sample. Because of the overlap of Ru $M_{4,5}$ edges with low-intensity Sr $M_{2,3}$, residual noticeable Sr signals remain when extracting the Ru signal. Black arrows in (a) and (c) point to regions with $n = 3$, which were observed occasionally in films prepared at optimal growth conditions.

Selected area STEM studies of these films corroborate the epitaxial orientations established by XRD and confirm that the growth occurred along the [001] direction with the c axis out of plane and the films being fully epitaxially strained to the $SrTiO_3$ substrate. The STEM images of two representatives $Sr_3Ru_2O_7$ films distinctly show the double-layered structure of the films, the interface between the substrate and deposited layers being coherent without misfit dislocations along the interface [Figs. 3(a) and 3(c)]. The annular dark-field [Fig. 3(b), center] and bright-field [Fig. 3(b), right] images show the Sr and Ru columns with enhanced atomic number contrast. The Ru atomic columns appear brightest due to the much higher atomic number of Ru compared with Sr, as also indicated in the inset with a superimposed structural model [Fig. 3(b)]. The alternate stacking of the rock salt SrO layers and the RuO_6 octahedra sheets observed in these images confirms the formation of the desired $n = 2$ member of the R-P structure. To evaluate the composition of the epitaxial $Sr_3Ru_2O_7$ films, electron energy-loss spectroscopy (EELS) measurements were performed on the cross section of the samples during STEM characterization. Figure 3(d) displays atomically resolved EELS elemental maps of a $Sr_3Ru_2O_7$

film. The black color suggests zero intensity, whereas the other colors indicate the expected chemical composition of different elements in the film (Ru, Sr, Ti, and O) that are resolved in the scanned region.

For epitaxial $Sr_3Ru_2O_7$ films grown at optimal growth conditions ($T_{sub} = 720\,°C$ and laser fluence = $2.5\,J/cm^2$), the defects detected are infrequently regions of $n = 3$ intergrowth within $n = 2$ layers [indicated by black arrows in Figs. 3(a) and 3(c)]. Such intergrowths were found in localized regions with insufficiently ordered volume to give rise to detectable diffraction spots in the XRD patterns. Similar intergrowth of extra n phases in R-P layers were reported in epitaxial films of $Sr_{n+1}Ru_nO_{3n+1}$ and $Sr_{n+1}Ti_nO_{3n+1}$ ($n = 2$ to 5) grown by MBE [10,25,48,50]. STEM investigations of films grown outside the optimal substrate temperature window showed increased defect density and populations of intergrowths of other n phases of the R-P series (see Fig. S1 within the SM [45]). These intergrowths are difficult to control in epitaxial growth using PLD. This is because minor stoichiometric deviations that can exist between the target and deposited films, together with the fact that the difference in the formation energies among nearby n members of the $Sr_{n+1}Ru_nO_{3n+1}$ series

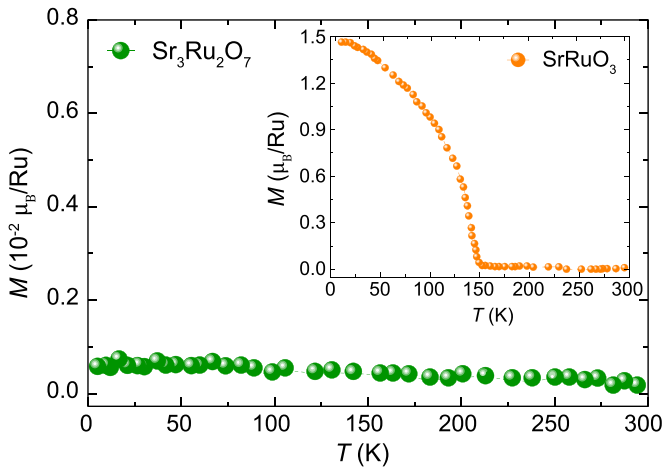FIG. 4. Magnetic ground state of $Sr_3Ru_2O_7$ films. Magnetization as a function of temperature of a typical $Sr_3Ru_2O_7$ film prepared at optimal growth conditions. For comparison, the magnetization data of a $SrRuO_3$ film is also presented in the inset.

is small, could lead to the formation of mixed *n*-phase films of these materials [49].

Magnetization as a function of temperature $M(T)$ of $Sr_3Ru_2O_7$ films were studied using a physical property

measurements systems (PPMS) vibrating sample magnetometer (VSM). The film was first precooled to 5 K while in a 0.1 T, and then warmed to 300 K in the presence of 0.01 T, the $M(T)$ data were collected. Figure 4 depicts the $M(T)$ curve (green) of a representative $Sr_3Ru_2O_7$ film grown on $SrTiO_3$ at the optimal growth conditions. These magnetization data are obtained after the subtraction of the diamagnetic contribution from the $SrTiO_3$ substrate. The $Sr_3Ru_2O_7$ films show no ferromagnetic transition, as the $M(T)$ curve is nearly flat in the measured temperature range. This observation is in agreement with previous reports on the magnetic ground state of epitaxial films of this material [25]. However, as it was expected, the $M(T)$ data of a $SrRuO_3$ control film prepared in the same PLD chamber show robust ferromagnetic ordering (see Fig. 4, inset), as revealed by a sharp paramagnetic to ferromagnetic transition at round 150 K, in agreement with previous reports [16,25,51]. Paramagnetic behavior has also been reported in $M(T)$ characteristics of high quality $Sr_3Ru_2O_7$ crystals grown by the floating zone technique, and a notable transition from paramagnetism to ferromagnetism was observed at ~70 K only under applied high pressure of ~1 GPa [26].

Figure 5(a) presents the temperature-dependent zero magnetic field sheet resistance (R_S) between 5 and 300 K for a 25-nm-thick unpatterned $Sr_3Ru_2O_7$ film and for two
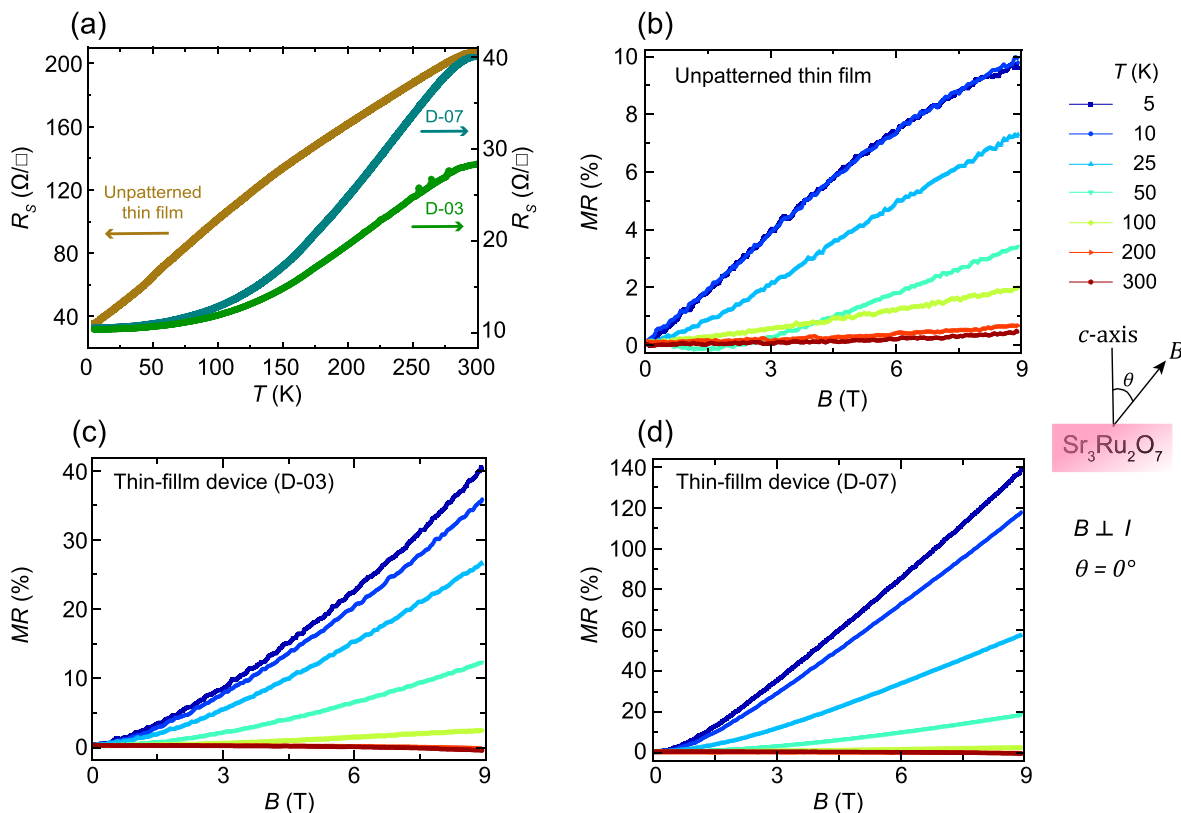

FIG. 5. Magnetotransport characteristics of a $Sr_3Ru_2O_7$ epitaxial film at various temperatures. (a) Temperature dependence of the zero-field sheet resistance (R_S) of a 25-nm-thick $Sr_3Ru_2O_7$ film before device fabrication (unpatterned thin film), and the R_S of two representative patterned Hall bar devices (D-03 and D-07) fabricated on the same $Sr_3Ru_2O_7$ film. The channel widths of D-03 and D-07 are 10 μm and 5 μm, respectively. (b) Magnetoresistance (MR) curves of a $Sr_3Ru_2O_7$ film measured at various temperatures in the Van der Pauw geometry before device fabrication (unpatterned thin film), and for (c) and (d) patterned Hall bar thin-film devices fabricated on the same film after measurements in the Van der Pauw configuration. MR data were acquired with $B \parallel c$ axis, $\theta = 0°$ (θ is the angle between the B field and c axis, as schematically illustrated in the right side of the figure).

representative patterned Hall bar devices fabricated side-by-side on this same film after Van der Pauw measurements. (For details on Hall bar devices, see Fig. S3 within the SM [45]). The unpatterned $Sr_3Ru_2O_7$ film and devices show metallic behavior over the entire temperature range. At 5 K, the R_S is roughly a factor of 4 higher in unpatterned film than in Hall bar devices. The extracted residual resistivity ratio (RRR), defined as $\rho(300\,\text{K})/\rho(5\,\text{K})$, is RRR $\simeq 6.8$ for 25-nm-thick films. This value is consistent with reported resistivity data of MBE-grown $Sr_3Ru_2O_7$ films of similar thickness [10]. From the temperature dependence of the normalized resistances, $R(T)/R(5\,\text{K})$, at various applied B-field orientations, the measured temperature dependence is isotropic in the absence of an applied field, while enhanced scattering is observed for in-plane applied B field of 5 T (see, Fig. S2 within the SM [45]). This enhanced scattering near the metamagnetic field transition was observed in a strained $Sr_3Ru_2O_7$ films [10], and it has been attributed to field-controlled instabilities of the Fermi surface of $Sr_3Ru_2O_7$ [31].

Figures 5(b)–5(d) show the MR at several temperatures for the same unpatterned film and two Hall bar devices fabricated on the same sample after measurements in Van der Pauw geometry. The magnetoresistance is defined as MR = $\left(\frac{R_{xx}(B)-R_{xx}(0)}{R_{xx}(0)}\right) \times 100$, where $R_{xx}(B)$ and $R_{xx}(0)$ are the longitudinal resistance measured at a field B and at zero field, respectively. MR data were acquired with the B field in out-of-plane direction ($B \parallel c$ axis, $\theta = 0°$), the excitation current being perpendicular to the field ($B \perp I$). No hysteresis loop was observed, which indicates that no intrinsic long-range ferromagnetic order occurs. Details on the analysis of MR data are discussed elsewhere [52–54].

For unpatterned films measured in Van der Pauw geometry at 5 K, a positive MR is measured at low magnetic fields together with a shallow change of slope slightly above 6 T [Fig. 5(b)]. As the temperature is increased further, this shallow slope at high B field disappears and MR data show quasi-quadratic field dependence. Positive MR with change of slope from a positive to a negative, resulting into a MR peak around 6 T, has been reported in thin $Sr_3Ru_2O_7$ single crystal nanosheets measured at 500 mK with $B \parallel c$ axis [30]. The positive MR peak has been associated with the metamagnetic transition in $Sr_3Ru_2O_7$ [27,30]. For patterned Hall bar devices, a positive and quasi-quadratic field dependence MR is observed independent of temperature [Figs. 5(c) and 5(d)]. Unlike for bulk crystals, we are not able to resolve a MR peak in $Sr_3Ru_2O_7$ thin films due most probably to impurity in these films, and also because MR data were acquired only down to 5 K and up to 9 T. For $Sr_3Ru_2O_7$ single crystals, a broad MR peak at 5 K was resolved only for MR data acquired up to 15 T [27].

The MR increases with decreasing temperature and it evolves into quasilinear behavior in the high-field limit. For the unpatterned $Sr_3Ru_2O_7$ film, a maximum MR ($T = 5\,\text{K}, B = 9\,\text{T}$) of 10% is obtained [Fig. 5(b)]. However, Hall bar devices fabricated on this same film show large positive MR values of 40% and 140% for devices of channel widths of 10 and 5 μm, respectively [Figs. 5(c) and 5(d)]. The positive MR for $B \parallel c$ is an indication of paramagnetic behavior of these films, which is consistent with known resistivity increase as magnetic field increases in most materials [55].
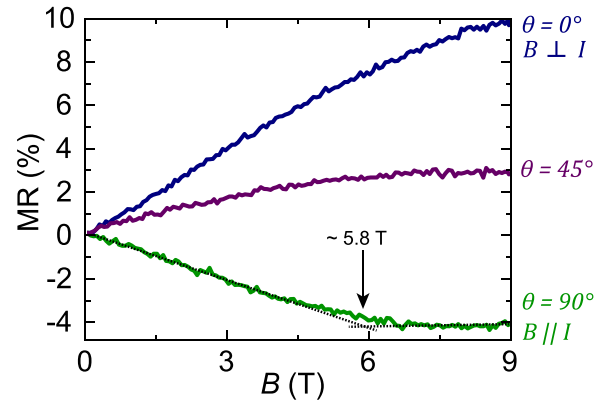

FIG. 6. MR characteristics at different B field orientation. The MR data of unpapatterned $Sr_3Ru_2O_7$ film were measured at 5 K in the Van der Pauw geometry. Linear fits (black dotted lines) on the MR curve for $\theta = 90°$ indicate a change of slope at a magnetic field of $\sim$5.8 T.

While for ferromagnets, MR is negative; for paramagnetic metals, the movement of carriers will be deflected under a Lorentz force, which increases the probability of carrier scattering, thereby increasing the resistance.

The differences revealed by the transport measurement results [Fig. 5(a)] and MR values of unpatterned films and patterned Hall bars [Figs. 5(b)–5(d)] is plausibly caused by inhomogeneities in the electron concentration caused by disorder in the sample. This will cause the bulk region to present different types of local current density and different potential landscape, resulting in different evolutions of the longitudinal potential profiles over certain portion of the film. We note that such types of inhomogeneities in disordered conductors is known to give rise to large MR, as described by the Parish and Littlewood model [56,57] that was used to explain large MR values in a range of materials (e.g., $Ag_{2\pm\delta}Te$, $Ag_{2\pm\delta}Se$, and Bi_2Te_3). In this case, the materials were modeled as a network of resistors due to disorder-induced mobility fluctuations [56,58,59]. For Hall bars of various channel widths structured on a $Sr_3Ru_2O_7$ film with some inhomogeneous disordered conduction (e.g., regions with higher conductivity than others), there will be inhomogeneity in the electron concentration over a small area in Hall bars, thus resulting in larger MR values in Hall bar devices as compared to unpatterned $Sr_3Ru_2O_7$ films. This interpretation is consistent to the observation that the Hall bar device with narrow channel width (D-07 of 5 μm width) exhibit large resistance and MR values as compared to the Hall bar device D-03 that has a channel width of 10 μm.

For the same film characterized in Fig. 5, we have performed angle dependence MR measurements at various temperatures. Figure 6 depicts representative MR data at 5 K for unpatterned $Sr_3Ru_2O_7$ film. The MR data were acquired for θ (the angle between the B field and the c axis of the sample) values of 0°, 45°, and 90°. As θ increases from 0° to 90°, the MR undergoes a gradual transition from positive to negative. For $\theta = 90°$, the MR is negative and it reaches a local minimum at a magnetic field of $\simeq$5.8 T, which is consistent with the in-plane metamagnetic transition behavior [10]. MR data of Hall bar device fabricated on the

same film exhibit qualitatively similar switching behaviors from positive to negative MR as the magnetic field is applied from out-of-plane ($B \parallel c$ axis) to in-plane direction ($B \parallel ab$ plane) (see Fig. S4 within the SM [45]). A maximum negative MR ($T = 5$ K, $B = 9$ T, $\theta = 90°$) values of –4% and –70% are obtained for unpatterned film (Fig. 6) and Hall bar device (see Fig. S4 within the SM [45]), respectively.

The observation of a negative MR at $\theta = 90°$, accompanied with a local minimum and shallow positive slope at high magnetic field, is attributed to the coexistence of short-range in-plane ferromagnetic order in the surface layer and metamagnetism in these films. The Ru^{4+} spin becomes aligned due to the applied magnetic field, thus spin-dependent scattering decreases, which gives rise to a negative MR. This observation is consistent with a recent magnetic field-controlled spectroscopic study that resolved in-plane ferromagnetism in $Sr_3Ru_2O_7$ single crystals that is sensitive to the direction of applied magnetic field [60]. Furthermore, we conjecture that the high MR values in these films could be due to spin fluctuations of the mobile electronic carriers when the material is under applied magnetic fields.

While nematic phases have been been reported in bulk single crystals of $Sr_3Ru_2O_7$ at low temperatures (<1 K) [8,61,62], there are no clear signatures of nematic phases detected in magnetotransport data of these PLD-grown films. The absence of nematic phase features in these epitaxial films is attributed to enhanced defect density, as evidenced by extracted RRR and TEM data. Further improvements of the crystalline quality of $Sr_3Ru_2O_7$ films, by reducing impurities and carrier scattering effects, will lead to an increase in RRR towards the bulk corresponding value of ~ 80 [26,30], as well as to the detection of clear signatures of novel emergent phenomena (e.g., nematic phase and non-Fermi-liquid behavior) in low-temperature magnetotransport data of $Sr_3Ru_2O_7$ films and patterned Hall bar devices.

In summary, we have explored an approach to stabilize the epitaxy of $Sr_3Ru_2O_7$ films by varying the substrate temperature and laser fluence in the PLD process, and investigated the magnetotransport trends in these epitaxial films. Structural characterizations of $Sr_3Ru_2O_7$ films prepared at optimal growth conditions confirm that these films are epitaxially oriented and nearly phase pure. Resistivity measurements of $Sr_3Ru_2O_7$ films and Hall bar devices exhibit characteristic metallic behavior. The magnetization characteristics of the films show no intrinsic ferromagnetic transition over the entire measured temperature range. These films exhibit a qualitatively similar MR behavior as previously reported for bulk single crystals and strained epitaxial films, specifically positive MR for the magnetic field applied along the c axis. However, we achieve unprecedented large magnetoresistance values up to 140% in Hall bar devices patterned on $Sr_3Ru_2O_7$ epitaxial films. Briefly, this paper is not only the reported effort for the epitaxial growth of nearly phase-pure $Sr_3Ru_2O_7$ films by PLD, but also explored the magnetotransport characteristics of a series of Hall bar devices patterned side-by-side on the same film, which help define a pathway towards understanding the synthesis science and device physics of epitaxial $Sr_3Ru_2O_7$ films. This provides an opportunity to explore more the physics of $Sr_3Ru_2O_7$-based devices for the realization and modulation of emergent phenomena at low temperatures in phase pure films. Based on these results, future directions are expected to focus on improving further the films quality and the investigation of magnetotransport properties of quantum structures (e.g., nonowires and quantum dots) patterned on epitaxial $Sr_{n+1}Ru_nO_{3n+1}$ films, as well as on nanoscale devices fabricated side-by-side on the same film in which magnetotransport properties can be modulated through quantum size effects and applied electric fields.

The data that support the findings of this study are available from the corresponding author upon reasonable request.

ACKNOWLEDGMENTS

[1] A. Chronister, A. Pustogow, N. Kikugawa, D. A. Sokolov, F. Jerzembeck, C. W. Hicks, A. P. Mackenzie, E. D. Bauer, and S. E. Brown, Proc. Natl. Acad. Sci. USA **118**, e2025313118 (2021).

[2] Z. Ali, M. Saghayezhian, Z. Wang, A. O'Hara, D. Shin, W. Ge, Y. T. Chan, Y. Zhu, W. Wu, S. T. Pantelides, and J. Zhang, npj Quantum Mater. **7**, 108 (2022).

[3] E. Dagotto, Science **309**, 257 (2005).

[4] S. A. Grigera, R. S. Perry, A. J. Schofield, M. Chiao, S. R. Julian, G. G. Lonzarich, S. I. Ikeda, Y. Maeno *et al.*, Science **294**, 329 (2001).

[5] Y. Maeno, H. Hashimoto, K. Yoshida, S. Nishizaki, T. Fujita, J. G. Bednorz, and F. Lichtenberg, Nature (London) **372**, 532 (1994).

[6] A. P. Mackenzie and Y. Maeno, Rev. Mod. Phys. **75**, 657 (2003), and references therein.

[7] S. A. Kivelson, A. C. Yuan, B. Ramshaw, and R. Thomale, npj Quantum Mater. **5**, 43 (2020).

[8] R. A. Borzi, S. A. Grigera, J. Farrell, R. S. Perry, S. J. S. Lister, S. L. Lee, D. A. Tennant, Y. Maeno, and A. P. Mackenzie, Science **315**, 214 (2007).

[9] S. Raghu, A. Paramekanti, E. A. Kim, R. A. Borzi, S. A. Grigera, A. P. Mackenzie, and S. A. Kivelson, Phys. Rev. B **79**, 214402 (2009).

[10] P. B. Marshall, K. Ahadi, H. Kim, and S. Stemmer, Phys. Rev. B **97**, 155160 (2018).

[11] P. Gegenwart, F. Weickert, M. Garst, R. S. Perry, and Y. Maeno, Phys. Rev. Lett. **96**, 136402 (2006).

[12] Y. J. Jo, L. Balicas, N. Kikugawa, E. S. Choi, K. Storr, M. Zhou, and Z. Q. Mao, Phys. Rev. B **75**, 094413 (2007).

[13] E. Carleschi, B. P. Doyle, R. Fittipaldi, V. Granata, A. M. Strydom, M. Cuoco, and A. Vecchione, Phys. Rev. B **90**, 205120 (2014).

[14] D. Fobes, T. J. Liu, Z. Qu, M. Zhou, J. Hooper, M. Salamon, and Z. Q. Mao, Phys. Rev. B **81**, 172402 (2010).

[15] P. Ngabonziza, J. D. Denlinger, A. V. Fedorov, G. Cao, J. W. Allen, G. Gebreyesus, and R. M. Martin, arXiv:2305.07222.

[16] G. Koster, L. Klein, W. Siemons, G. Rijnders, J. S. Dodge, C.-B. Eom, D. H. A. Blank, and M. R. Beasley, Rev. Mod. Phys. **84**, 253 (2012), and references therein.

[17] S. Hahn, B. Sohn, M. Kim, J. R. Kim, S. Huh, Y. Kim, W. Kyung, M. Kim, D. Kim, Y. Kim, T. W. Noh, J. H. Shim, and C. Kim, Phys. Rev. Lett. **127**, 256401 (2021).

[18] M. Kim and B. I. Min, Phys. Rev. B **91**, 205116 (2015).

[19] H. Boschker, T. Harada, T. Asaba, R. Ashoori, A. V. Boris, H. Hilgenkamp, C. R. Hughes, M. E. Holtz, L. Li, D. A. Muller, H. Nair, P. Reith, X. Renshaw Wang, D. G. Schlom, A. Soukiassian, and J. Mannhart, Phys. Rev. X **9**, 011027 (2019).

[20] H. P. Nair, J. P. Ruf, N. J. Schreiber, L. Miao, M. L. Grandon, D. J. Baek, B. H. Goodge, J. P. C. Ruff, L. F. Kourkoutis, K. M. Shen, and D. G. Schlom, APL Mater. **6**, 101108 (2018).

[21] Y. Fang, H. P. Nair, L. Miao, B. Goodge, N. J. Schreiber, J. P. Ruf, L. F. Kourkoutis, K. M. Shen, D. G. Schlom, and B. J. Ramshaw, Phys. Rev. B **104**, 045152 (2021).

[22] P. Ngabonziza, Y. Wang, P. A. van Aken, J. Maier, and J. Mannhart, Adv. Mater. **33**, 2007299 (2021).

[23] S. Kaneta-Takada, Y. K. Wakabayashi, Y. Krockenberger, T. Nomura, Y. Kohama, S. A. Nikolaev, H. Das, H. Irie, K. Takiguchi, S. Ohya *et al.*, npj Quantum Mater. **7**, 102 (2022).

[24] K. Takiguchi, Y. K. Wakabayashi, H. Irie, Y. Krockenberger, T. Otsuka, H. Sawada, S. A. Nikolaev, H. Das, M. Tanaka, Y. Taniyasu, and H. Yamamoto, Nat. Commun. **11**, 4969 (2020).

[25] W. Tian, J. H. Haeni, D. G. Schlom, E. Hutchinson, B. L. Sheu, M. M. Rosario, P. Schiffer, Y. Liu, M. A. Zurbuchen, and X. Q. Pan, Appl. Phys. Lett. **90**, 022507 (2007).

[26] S.-I. Ikeda, Y. Maeno, S. Nakatsuji, M. Kosaka, and Y. Uwatoko, Phys. Rev. B **62**, R6089(R) (2000).

[27] R. S. Perry, L. M. Galvin, S. A. Grigera, L. Capogna, A. J. Schofield, A. P. Mackenzie, M. Chiao, S. R. Julian, S. I. Ikeda, S. Nakatsuji, Y. Maeno, and C. Pfleiderer, Phys. Rev. Lett. **86**, 2661 (2001).

[28] E. Ohmichi, Y. Yoshida, S. I. Ikeda, N. V. Mushunikov, T. Goto, and T. Osada, Phys. Rev. B **67**, 024432 (2003).

[29] S. A. Grigera, P. Gegenwart, R. A. Borzi, F. Weickert, A. J. Schofield, R. S. Perry, T. Tayama, T. Sakakibara, Y. Maeno, A. G. Green, and A. P. Mackenzie, Science **306**, 1154 (2004).

[30] W. Chu, N. Wang, Y. Liu, Y. Wang, G. Liu, Y. Han, N. Hao, Z. Qu, J. Yang, F. Xue, Z. Mao, and M. Tian, Phys. Rev. B **102**, 195119 (2020).

[31] A. Tamai, M. P. Allan, J. F. Mercure, W. Meevasana, R. Dunkel, D. H. Lu, R. S. Perry, A. P. Mackenzie, D. J. Singh, Z.-X. Shen, and F. Baumberger, Phys. Rev. Lett. **101**, 026407 (2008).

[32] V. Shaginyan, A. Msezane, K. Popov, J. Clark, M. Zverev, and V. Khodel, Phys. Lett. A **377**, 2800 (2013).

[33] P. Ngabonziza, E. Carleschi, V. Zabolotnyy, A. Taleb-Ibrahimi, F. Bertran, R. Fittipaldi, V. Granata, M. Cuoco, A. Vecchione, and B. P. Doyle, Sci. Rep. **10**, 21062 (2020).

[34] G. Gebreyesus, P. Ngabonziza, J. Nagura, N. Seriani, O. Akin-Ojo, and R. M. Martin, Phys. Rev. B **105**, 165119 (2022).

[35] I. Benedičič, M. Naritsuka, L. C. Rhodes, C. Trainer, Y. Nanao, A. B. Naden, R. Fittipaldi, V. Granata, M. Lettieri, A. Vecchione, and P. Wahl, Phys. Rev. B **106**, L241107 (2022).

[36] E. Fradkin, S. A. Kivelson, M. J. Lawler, J. P. Eisenstein, and A. P. Mackenzie, Annu. Rev. Condens. Matter Phys. **1**, 153 (2010), and references therein.

[37] J. Hooper, M. Zhou, Z. Mao, R. Perry, and Y. Maeno, Phys. Rev. B **72**, 134417 (2005).

[38] W. Braun, M. Jäger, G. Laskin, P. Ngabonziza, W. Voesch, P. Wittlich, and J. Mannhart, APL Mater. **8**, 071112 (2020).

[39] A stoichiometric PLD target of $Sr_3Ru_2O_7$ was obtained from Toshima Manufacturing Co., Ltd. http://www.material-sys.com/ (accessed: Setpember 2023). Using a stoichiometric $SrRuO_3$ PLD target obtained from the same supplier, we also made control films of $SrRuO_3$.

[40] Q. Huang, J. W. Lynn, R. W. Erwin, J. Jarupatrakorn, and R. J. Cava, Phys. Rev. B **58**, 8515 (1998).

[41] N. Aso, Y. Uwatoko, H. Kimura, Y. Noda, Y. Yoshida, S.-I. Ikeda, and S. Katano, J. Phys.: Condens. Matter **17**, S3025 (2005).

[42] H. Shaked, J. Jorgensen, O. Chmaissem, S. Ikeda, and Y. Maeno, J. Solid State Chem. **154**, 361 (2000).

[43] M. Uchida, M. Ide, H. Watanabe, K. S. Takahashi, Y. Tokura, and M. Kawasaki, APL Mater. **5**, 106108 (2017).

[44] J. Kim, J. Mun, C. M. Palomares García, B. Kim, R. S. Perry, Y. Jo, H. Im, H. G. Lee, E. K. Ko, S. H. Chang *et al.*, Nano Lett. **21**, 4185 (2021).

[45] See Supplemental Material at http://link.aps.org/supplemental/10.1103/PhysRevMaterials.8.044401 for additional microstructural characterizations using TEM, and device patterning using electron beam lithography, as well as electronic transport characteristics of epitaxial $Sr_3Ru_2O_7$ films prepared at the optimal growth conditions and extra magnetotransport data of epitaxial $Sr_3Ru_2O_7$ films.

[46] A. M. Miller, M. Lemon, M. A. Choffel, S. R. Rich, F. Harvel, and D. C. Johnson, Z. Naturforsch. B **77**, 313 (2022).

[47] Since $SrRuO_3$ has the most thermodynamically stable phase in the $Sr_{n+1}Ru_nO_{3n+1}$ series [63], control films of $SrRuO_3$ [39] were used to trace possible intergrowth phases and change of stability in $Sr_3Ru_2O_7$ films. Control samples of $SrRuO_3$ were grown at a substrate temperature of $680°C$ and laser fluence of $2\,J\,cm^{-2}$.

[48] J. H. Haeni, C. D. Theis, D. G. Schlom, W. Tian, X. Q. Pan, H. Chang, I. Takeuchi, and X.-D. Xiang, Appl. Phys. Lett. **78**, 3292 (2001).

[49] E. E. Fleck, M. R. Barone, H. P. Nair, N. J. Schreiber, N. M. Dawley, D. G. Schlom, B. H. Goodge, and L. F. Kourkoutis, Nano Lett. **22**, 10095 (2022).

[50] W. Tian, X. Q. Pan, J. H. Haeni, and D. G. Schlom, J. Mater. Res. **16**, 2013 (2001).

[51] G. Laskin, H. Wang, H. Boschker, W. Braun, V. Srot, P. A. van Aken, and J. Mannhart, Nano Lett. **19**, 1131 (2019).

[52] P. Ngabonziza, Nanotechnology **33**, 192001 (2022).

[53] P. Ngabonziza, Y. Wang, and A. Brinkman, Phys. Rev. Mater. **2**, 044204 (2018).

[54] M. P. Stehno, P. Ngabonziza, H. Myoren, and A. Brinkman, Adv. Mater. **32**, 1908351 (2020).

[55] R. Niu and W. K. Zhu, J. Condens. Matter Phys. **34**, 113001 (2022).

[56] M. M. Parish and P. B. Littlewood, Nature (London) **426**, 162 (2003).

[57] M. M. Parish and P. B. Littlewood, Phys. Rev. B **72**, 094417 (2005).

[58] D. P. Leusink, R. G. J. Smits, P. Ngabonziza, X. L. Wang, S. Wiedmann, U. Zeitler, and A. Brinkman, arXiv:1412.4065.

[59] J. C. de Boer, D. P. Leusink, and A. Brinkman, J. Phys. Commun. **3**, 115021 (2019).

[60] M. Naritsuka, I. Benediči, L. C. Rhodes, C. A. Marques, C. Trainer, Z. Li, A. C. Komarek, and P. Wahl, Proc. Natl. Acad. Sci. USA **120**, e2308972120 (2023).

[61] J. A. N. Bruin, R. A. Borzi, S. A. Grigera, A. W. Rost, R. S. Perry, and A. P. Mackenzie, Phys. Rev. B **87**, 161106(R) (2013).

[62] C. Stingl, R. S. Perry, Y. Maeno, and P. Gegenwart, Phys. Rev. Lett. **107**, 026404 (2011).

[63] H. P. Nair, Y. Liu, J. P. Ruf, N. J. Schreiber, S.-L. Shang, D. J. Baek, B. H. Goodge, L. F. Kourkoutis, Z.-K. Liu, K. M. Shen, and D. G. Schlom, APL Mater. **6**, 046101 (2018).